Detection of Geothermal Anomaly Areas With Spatio-Temporal Analysis Using Multitemporal Remote Sensing Data

Shanwei Liu, Chuanlong Ye, Qinting Sun, Mingming Xu, *Member, IEEE*, Zhongfeng Duan, Hui Sheng, and Jianhua Wan

***Abstract*—Thermal infrared (TIR) remote sensing is an important technology for detecting geothermal anomalies. However, detection results have been found to have a certain dependency on the distribution of ground objects and imaging conditions at different times, and pseudo-anomalous areas are easily extracted. To solve this problem, a new geothermal anomaly detection method is proposed in this article and implemented in the Jiaonan uplift in the Yishu fault zone. A temperature inversion experiment is carried out on TIR remote sensing images based on the radiation transfer equation. Then, a gradient operator is used to extract high-temperature regions in various periods, and geothermal anomaly areas are selected through the spatio-temporal analysis method proposed in this article after excluding the influence of impervious surfaces, water bodies, and vegetation. The temperature anomaly points, which are all high-temperature points in each inversion result and geothermal anomaly areas extracted by the proposed method, are compared with the five geothermal anomaly points, which are determined based on 150 geothermal wells and the geological structure in the study area. The spatial locations of the temperature anomaly points and geothermal anomaly areas are close to those of the geothermal anomaly points. Compared with the mean grad method, the proposed method is found to effectively delete some pseudo-anomaly areas under the premise of ensuring the extraction accuracy of geothermal anomaly areas.**

***Index Terms*—Geothermal anomaly, temperature inversion, thermal infrared remote sensing data.**

I. Introduction

GEOTHERMAL energy is the energy contained in the earth's interior in the form of heat. Compared with traditional fossil fuel energy, it has the advantages of being renewable and widely distributed and having rich reserves and a low cost per unit. It has now become a major energy source for life on earth [1], [2]. Combined with the local geological structure, the groundwater temperature in geothermal wells is used to determine the geothermal anomaly areas in traditional geothermal detection methods. This method is a destructive way to detect geothermal anomaly areas, and it is limited to inferring all geothermal anomaly areas by using local temperature points [3], [4]. As a unique tool, thermal infrared (TIR) remote sensing has been gradually applied to geothermal detection due to its advantages of synchronous observations over large areas, convenient data acquisition, and low experimental cost [5]–[7].

Land surface temperature (LST) is important indirect evidence of geothermal anomalies [8]. TIR remote sensing surveys can detect very small temperature anomalies ranging from 0.05 to 0.5°C within a range of hundreds of square kilometers [9]. Therefore, based on the excellent performance of TIR remote sensing for surface temperature detection, this method can be used to detect geothermal and inverse temperatures [7], [8], [10]–[15]. Among these literature, most studies determine geothermal anomaly areas by combining LST inversed from signal-temporal satellite data and local geological structure or other geological data [9], [16]–[20]. To obtain more accurate geothermal anomaly areas, unmanned aerial vehicles (UAVs) replace satellites as a new means to collect higher resolution surface temperature data and have achieved good experimental results [21]–[23]. When the LST inversion algorithm is used to detect geothermal anomaly areas, many factors will affect the accuracy of geothermal detection. To ensure the extraction of geothermal anomaly areas, scholars adopt a variety of methods to eliminate pseudo-anomalies, including using night remote sensing data [24] and thermal inertia correction [6] and considering ground objects and topographic factors [25].

Geothermal energy, excluding the case of overexploitation by humans, should be relatively stable; that is, it can persist for a long time. Multitemporal remote sensing images can be used for geothermal anomaly detection by choosing stable high-temperature areas as geothermal anomaly areas so that the geothermal determination results based on multitemporal TIR remote sensing data are more reliable and better conform to geothermal characteristics than those based on single-temporal TIR remote sensing data. Some scholars use multitemporal TIR remote sensing data for geothermal anomaly detection and geothermal research. Among these approaches, the main method

Manuscript received January 16, 2021; revised April 12, 2021; accepted April 24, 2021. Date of publication April 27, 2021; date of current version May 26, 2021. This work was supported by the National Natural Science Foundation of China under Grant 41776182 and Grant 42072234. *(Corresponding author: Jianhua Wan.)*

Shanwei Liu, Chuanlong Ye, Mingming Xu, Hui Sheng, and Jianhua Wan are with the College of Oceanography and Space Informatics, China University of Petroleum (East China), Qingdao 266580, China (e-mail: shanweiliu@163.com; z19160002@s.upc.edu.cn; xumingming@upc.edu.cn; sheng@upc.edu.cn; wjh66310@163.com).

Qinting Sun and Zhongfeng Duan are with the School of Geosciences, China University of Petroleum (East China), Qingdao 266580, China (e-mail: s16010068@s.upc.edu.cn; duanzf@upc.edu.cn).

Digital Object Identifier 10.1109/JSTARS.2021.3076162

uses the multitemporal LST inversion results and the geological structure in the study area for analysis to obtain the geothermal anomaly area [26], [27]. However, this method does not make full use of multitemporal TIR remote sensing image data and does not have a specific process for extracting geothermal anomaly areas. At the same time, some scholars proposed other geothermal anomaly extraction algorithms based on multitemporal remote sensing data, including the clustering [28], the multitemporal mean method [29], and the mean grad method [30]. However, most of the current methods have difficulty deleting unstable geothermal anomalies and pseudo-anomaly areas.

Based on the above content, this article proposes a method for geothermal detection based on spatio-temporal analysis can effectively eliminate unstable geothermal anomalies and pseudo-anomaly areas during the geothermal extraction process. This algorithm is easy to implement and understand to detect geothermal anomaly areas based on multitemporal remote sensing data. The algorithm is based on multitemporal Landsat 8 remote sensing satellite images for temperature inversion. After excluding the influence of impervious surfaces, water bodies and vegetation, the areas with high-temperature anomalies at all-time points are selected as the geothermal anomaly areas through regional superposition. In this article, the method is applied to the Jiaonan uplift area in the Yishu fault zone and compared with the mean grad method. The geothermal anomaly area is delineated based on the proposed method, and the results are verified by combining the temperature anomaly points determined based on visual interpretation and the geothermal anomaly points based on field experiments. Finally, we analyze the geological structure of the region, explain the formation of the geothermal anomalies and compare the results with those of another method.

The remainder of this article is organized as follows. The Section II introduces the research area of this article. Section III introduces the experimental data and the experimental process of geothermal anomaly extraction. Section IV is the detailed operational process of the experimental results. Section V is a discussion of the experimental results, and the finally, Section VI summarizes this article.

II. Study Area

The Yishu fault zone is part of the Tanlu fault zone that passes through Shandong. It is also the section where the tectonic profile is best exposed and the neotectonic activity is the strongest. During its long-term activity, the main section has exhibited different mechanical properties. The early extensional activity formed a wide fracture zone and triggered Cretaceous volcanic eruptions and fault depression. The Mesozoic was an important turning point in the history of the geological development of the Yishu fault zone. Due to the intensified activity of the Yishu rift, a small amount of diorite porphyrite was emplaced along the fault, which triggered volcanic activity and formed a large area of andesite coverage. By the Late Cretaceous, the activity tended to stop. Since the Cenozoic and Tertiary, the Yishu fault zone has shown strong compression and formed a series of compressive structures. The main section is subjected to mechanical compression and torsion, and its hydrogeological properties show both water resistance and heat insulation [7], [31], [32]. The Yishu fault consists of four main fault zones. On both sides of each main fault, there are multiple near-parallel secondary faults of different sizes that form fault bundles, which together form the complex Yishu fault zone. At present, many geothermal resources have been discovered in the Jiaonan uplift area within the Yishu fault zone. However, due to long-term overexploitation, geothermal resources are on the verge of exhaustion. Studying the spatial distribution of geothermal resources in the subregions of the Jiaonan uplift, delineating the scope of geothermal anomaly areas, and evaluating the reserves of geothermal resources are of great significance for the rational development of geothermal resources in the region.

The research area of this experiment is located in the Jiaonan uplift area of the Yishu fault zone, which is found in Rizhao city. The extreme geographic coordinates are $35°22'58''\sim35°51'48''$ north latitude and $119°03'53''\sim119°33'31''$ east longitude, and the area is approximately 1161 km^2. The terrain of the study area is high in the middle and low on all sides, slightly inclined to the southeast, and distributed among mountains, hills, and plains. Fig. 1 shows the approximate geographical location of the study area.

III. Materials and Methods

A. Materials

1) Primary Data: In this study, we used standard terrain correction (Level 1T) data from the Operational Land Imager (OLI), a nine-channel push-broom sensor with a spatial resolution of 30 m (15 m for panchromatic channel 8), and a single scene size of 185 $\times$ 180 km, which matches the second global reference system [33], [34].

2) Secondary Data: In this experiment, relevant regional data such as the water system, settlements, and infrastructure of the study area were collected, as shown in Fig. 2. By considering the geographical factors and geological structure in the study area, 150 geothermal wells were established for delineation of geothermal anomaly areas. The geothermal gradient contour map of the study area is drawn based on the above geothermal wells and is shown in Fig. 3. Geothermal areas generally occur in places with high temperature gradients and extend along the direction of faults. Based on the above characteristics, we chose five geothermal anomaly points after a comprehensive analysis of the geothermal gradient contour map and geological structure. The specific geographical distribution of the geothermal anomaly points is shown in Fig. 3.

B. Methods

This study is divided into four main parts. First, the remote sensing data are preprocessed, mainly for radiometric calibration and atmospheric correction of the Landsat 8 remote sensing images. The second step is to retrieve the temperature of the study area based on the radiative transfer equation using Landsat 8 multitemporal TIR remote sensing images. The third step is to classify the research area to eliminate the influence of

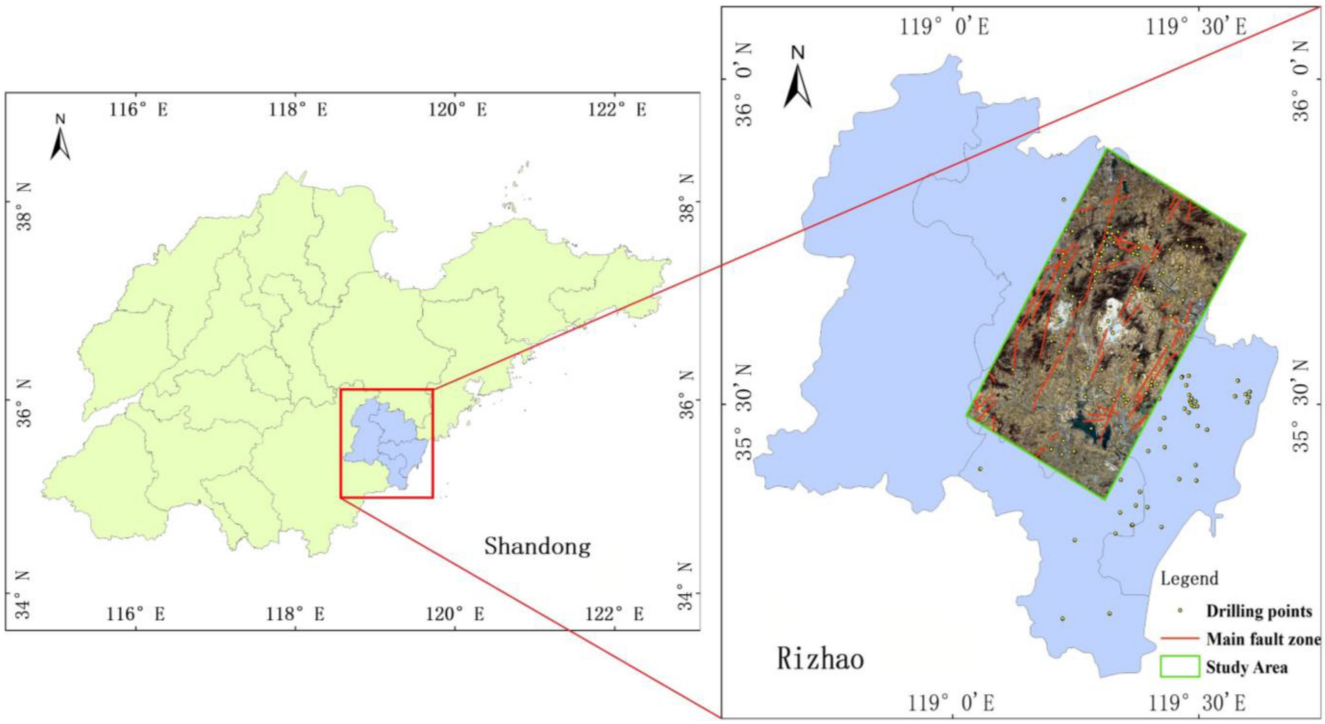

Fig. 1. Geographical location map of the study area.

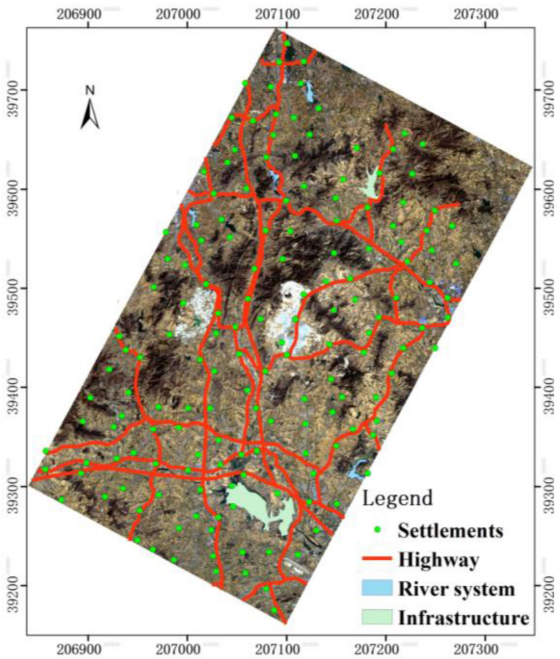

Fig. 2. Locations of settlements, mountains, roads, water systems, and infrastructure in the study area.

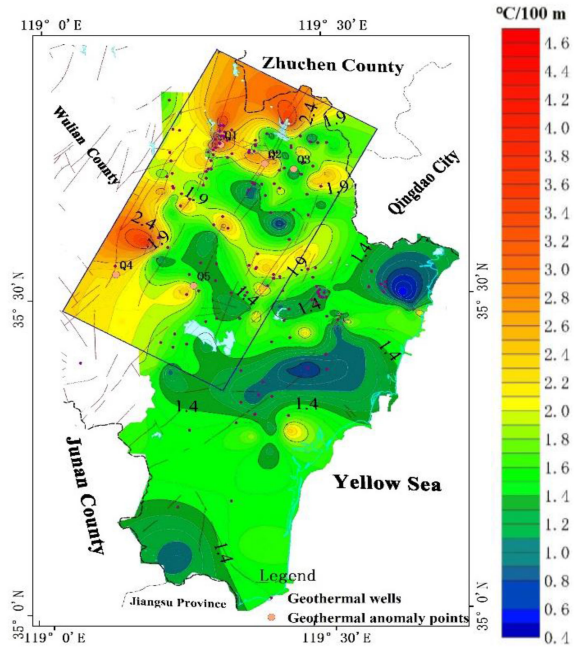

Fig. 3. Geothermal gradient contour map of the study area.

impervious surfaces such as buildings, roads, and water bodies on the extraction of geothermal anomaly areas. Finally, the temperature anomaly points and geothermal anomaly areas are delineated according to the distribution of the surface features and long-term temperature inversion results. The specific experimental flow chart for this study is shown in Fig. 4.

1) Image Preprocessing: The digital number (DN) obtained by remote sensing images is not convenient for multitemporal remote sensing image experiments, so it needs to be converted

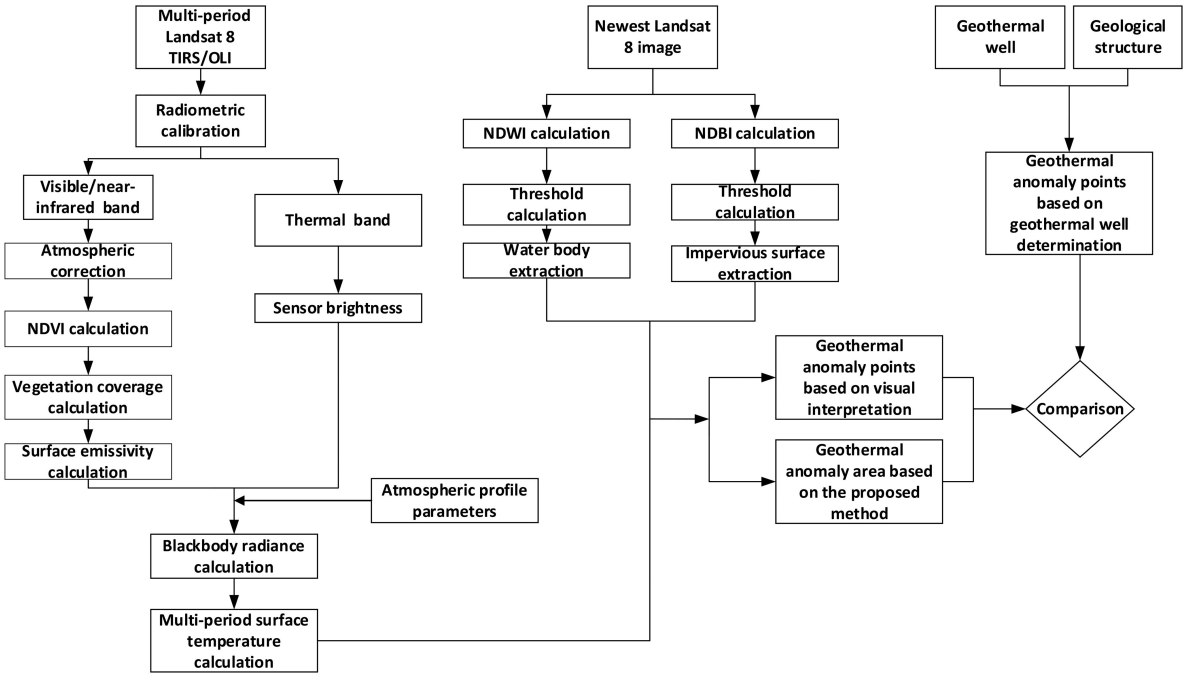

Fig. 4. General flowchart of the methods used in this study.

into absolute radiance according to radiometric calibration. The Landsat 8 remote sensing images are calibrated in this article; among them, the DN value is converted to a radiance value according to (1)

$$L_\lambda = M_L \cdot Q_{\text{cal}} + A_L \tag{1}$$

where L_λ is the spectral radiance [(W/(m2·sr μm)], M_λ is the radiance multiplicative scaling factor, A_L is the radiation additive scaling factor, all of which were provided by the United States Geological Survey, and $Q_{\text{cal}}$is the DN value of each band in the image.

Solar radiation is incident on the surface of the object in a certain way through the atmosphere and then reflects back to the sensor. Due to the influence of atmospheric aerosols, terrain, and nearby features, the original image contains a combination of information about the surface of the object, the atmosphere, and the sun. If we want to understand the spectral properties of an object's surface, we must separate its reflection information from the information about the atmosphere and the sun, which requires an atmospheric correction process to eliminate the influence of factors such as atmosphere and light on the reflection of ground objects. In this article, the fast line-of-sight atmospheric analysis of hypercubes model is used for atmospheric correction.

2) Surface Temperature Calculation: Common algorithms for Landsat 8 temperature inversion include the mono-window algorithm [35], split-window algorithm [36], and radiative transfer equation [37]. Experiments show that among the three methods, the experimental results obtained by using the radiative transfer equation for temperature inversion are the most accurate [38], [39]. The basic principle of the temperature inversion method based on the radiative transfer equation is as follows: the effect of thermal radiation of the earth's surface atmosphere is estimated first, and the influence of the satellite sensors minus the amount of heat radiation observed and the surface thermal radiation intensity is then subtracted. Combining these values, the thermal radiation intensity is converted to the corresponding surface temperature, and the experimental process is as follows.

i) Emissivity Calculation

Emissivity is an important parameter in the surface temperature inversion process. In this article, the surface emissivity is derived by calculating the value of the normalized difference vegetation index (NDVI) [40]. Equation (2) is used to compute the NDVI from the atmosphere-corrected red reflectance (ρ_{red}) and near-infrared reflectance (ρ_{nir}) from the OLI data. Vegetation coverage is an intermediate variable for calculating the surface radiation ratio, and the calculation is via (3)

$$\text{NDVI} = \frac{\rho_{\text{nir}} - \rho_{\text{red}}}{\rho_{\text{nir}} + \rho_{\text{red}}} \tag{2}$$

$$Pv = \left(\frac{\text{NDVI} - \text{NDVI}_s}{\text{NDVI}_v - \text{NDVI}_s}\right)^2 \tag{3}$$

where NDVI_s is the NDVI value of the pixel completely covered by bare land and NDVI_v represents the NDVI value of the pixel completely covered by vegetation, that is, the NDVI value of the pure vegetation pixel. We take NDVI_v as 0.65 and NDVI_s as 0.2; that is, when the NDVI of a pixel is greater than 0.60, the *Pv* value is 1, and its surface emissivity is 0.99; if the NDVI of a pixel is less than 0.05, the *Pv* value is 0, and its surface reflectivity is 0.97 [40]; when the NDVI of a pixel is between 0.05 and 0.60, the *Pv* value is calculated by (3), and the surface reflectivity can be obtained according to (4) [41]

$$\varepsilon = 0.004 \times Pv + 0.986. \tag{4}$$

ii) Land Surface Temperature Calculation

Based on the radiative transfer equation [38], the TIR radiance value L_Z received by the satellite sensor is divided into three parts: the energy of the upward radiant brightness of the atmosphere, the energy of the true radiance of the ground reaching the satellite sensor after passing through the atmosphere, and the downward radiant energy of the atmosphere. The energy is reflected in the sensor after radiation reaches the ground. Equation (5) is used to calculate the TIR radiance value received by the satellite sensor

$$LZ = [\varepsilon B(TS) + (1-\varepsilon)Ld]\tau + LU \tag{5}$$

where T_S represents the real surface temperature (K), $B(T_S)$ is the blackbody radiation, and τ is the transmittance of the TIR band, which can be obtained from the NASA website[1] together with L_U and L_d. Equations. (6) and (7) are used for measuring T_S

$$B\left(T_S\right) = [L_Z - L_U - \tau(1-\varepsilon)L_d]/\tau\varepsilon \tag{6}$$

$$T_S = K_2/In(K_1/B\left(T_S\right) + 1) \tag{7}$$

where $K_1 = 774.89$ W/(m^2 *um sr*) and $K_2 = 1321.08$ *K*.

3) Classification: There are many sources of abnormal temperatures that can interfere with the thermal anomalies caused by faults and fractures. Such variations are always caused by the distribution of surface features in the study area; for example, the temperature of a water body is lower than that of bare land, so it is easy to regard areas around water bodies as temperature anomalies when identifying temperature anomaly areas. Constructing geothermal wells near water bodies is not easy under normal circumstances; thus, verifying whether the area around water body represents a geothermal anomaly is difficult. Therefore, in this experiment, water bodies are directly excluded. In general, the temperature of the impervious surface of buildings and roads is higher than that of bare land, and the reason for this difference is only that the reflectances of impervious surfaces and bare land are different, which is called an artificial geothermal phenomenon. In the experiment, impervious surfaces also need to be removed to decrease error.

In this study, the normalized difference water index (NDWI) and normalized difference built-up index (NDBI) are used to obtain relevant greyscale images of water bodies and impervious surfaces in the study area. OLI Bands 4 (ρ_{red}) and 5 (ρ_{nir}) are used in (8) to calculate NDWI; OLI Bands 7 (ρ_{mir}) and 5 (ρ_{nir}) are used in (9) to calculate the NDBI. After obtaining the greyscale images of water bodies and buildings, the adaptive threshold method is used to set appropriate thresholds, and water bodies and buildings in the study area are then extracted[42]

$$\mathrm{NDWI} = \frac{\rho_{\mathrm{Green}} - \rho_{\mathrm{Nir}}}{\rho_{\mathrm{Green}} + \rho_{\mathrm{Nir}}} \tag{8}$$

$$\mathrm{NDBI} = \frac{\rho_{\mathrm{Mir}} - \rho_{\mathrm{Nir}}}{\rho_{\mathrm{Mir}} + \rho_{\mathrm{Nir}}}. \tag{9}$$

When the threshold method is used to extract impervious surfaces in the research area, some impervious surfaces may be missed. Therefore, visual interpretation is necessary after using the NDBI to extract buildings to reduce the impact of buildings.

In addition to water bodies and impervious surfaces, vegetation and soil are the main ground features in the study area. Vegetation coverage and sun exposure will interfere with the detection of geothermal anomaly areas [19], [43], and it is difficult to distinguish between vegetation and soil using existing methods. To avoid the difficulty of distinguishing between vegetation and soil, this article chooses autumn and winter Landsat 8 remote sensing image data. During this period, the vegetation in the study area is sparse, and the sun is relatively weak, which not only solves the problem of indistinguishability between vegetation and soil but also reduces the error in detecting geothermal anomalies caused by the sun.

4) Extraction of Geothermal Anomaly Areas: Features in the study area are classified based on a previous step to obtain the distribution of features. The regions of impervious surfaces and water bodies are removed from the temperature inversion results of each period, and the gradient operator is then used to process each temperature inversion result to obtain the temperature anomaly areas at each time. In this article, spatio-temporal analysis is used for geothermal anomaly detection. The temperature anomaly areas at a certain time are selected as the preliminary geothermal anomaly areas, and the preliminary geothermal anomaly areas are spatially superimposed with the temperature anomaly areas at another time. If the subregions overlap, they are merged as a new geothermal anomaly area; otherwise, the temperature anomaly subarea is deleted. Through the above operation, this method can eliminate the pseudo-anomaly areas caused by the distribution of ground objects and some unstable geothermal anomaly regions. The purpose of this method is to extract the geothermal anomaly regions that are characterized by high-temperature anomalies in each period. The flow diagram is shown in Fig. 5. This process is repeated until the temperature anomaly areas of all the remaining periods are traversed, and the final geothermal anomaly areas are obtained.

IV. Experiment

A. Satellite Image Preprocessing

The remote sensing images selected in this experiment are the Landsat 8 remote sensing images in row 120 and column 35 taken on December 1, 2013; April 24, 2014; November 8, 2014; March 31, 2017; and February 1, 2019. Radiation calibration and atmospheric correction are carried out on Landsat 8 remote sensing images at various time points, and the DN value of each band is converted into a radiation value. The bands are Band 3 (green), Band 4 (red), Band 5 (NIR), Band 7 (mid-infrared, MIR), and Band 10 (TIR), which are needed in the next experiment. The remote sensing images of each period are clipped to obtain the images of the research area at each time point.

B. Temperature Inversion Results

According to the above steps of LST calculation, the temperature results for the five study periods can be obtained as shown in Fig. 6.

[1] Online. [Available]: http://atmcorr.gsfc.nasa.gov/

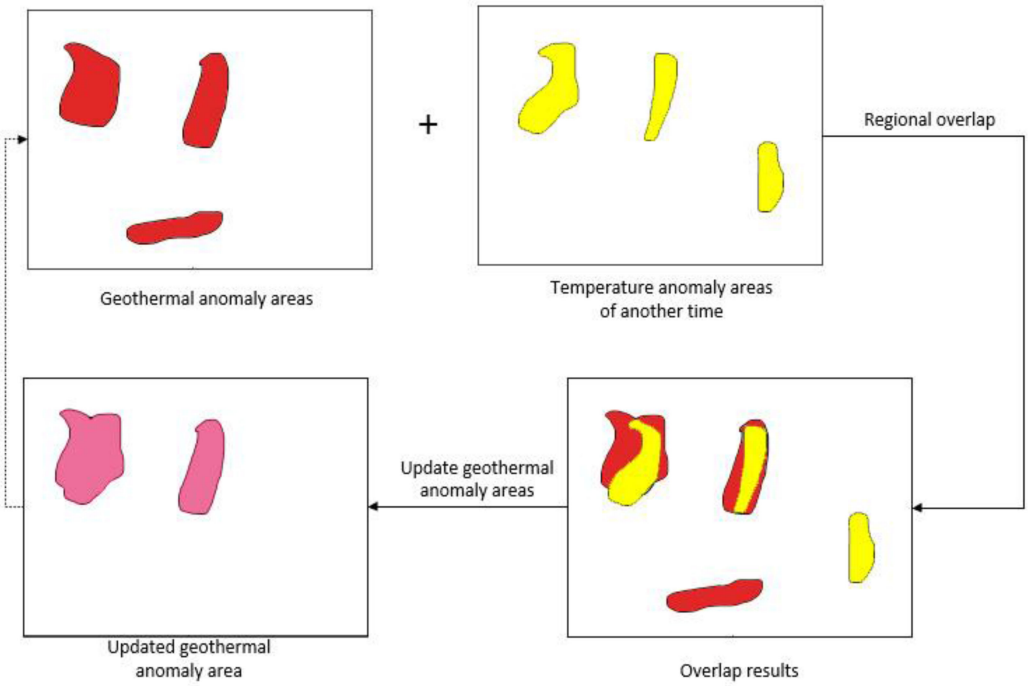

Fig. 5. Schematic diagram of the selection of abnormal geothermal areas.

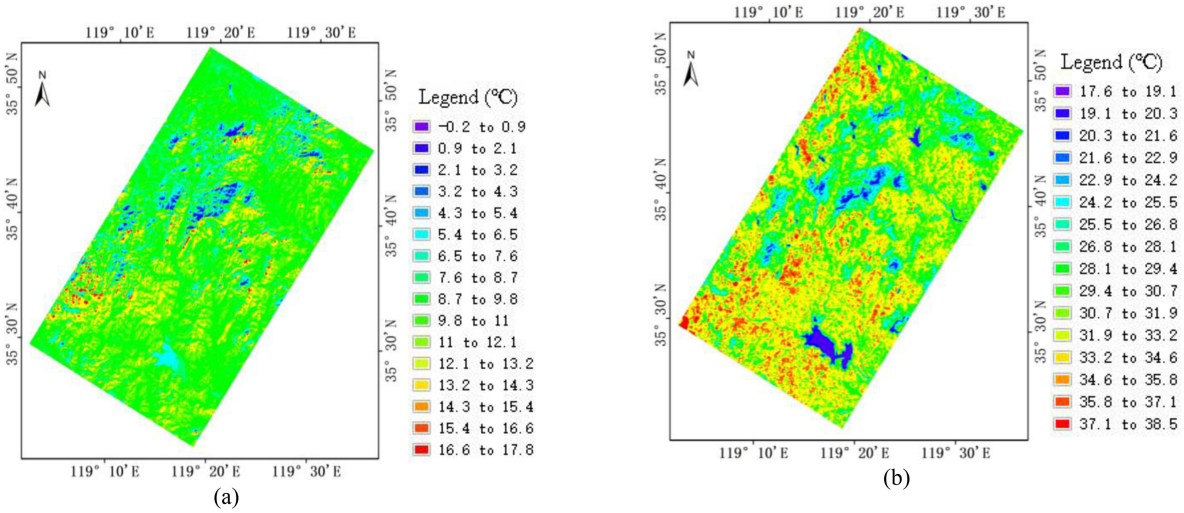

Fig. 6. Temperature inversion results for each period. (a) Inversion results for December 1, 2013. (b) Inversion results for April 24, 2014.

Fig. 6 shows that the temperature fluctuation range at each time point is relatively large. The minimum temperature difference for February 1, 2019, is 16.4°C. On April 24, 2012, the temperature difference in the study area is the largest, reaching 20.9°C. The main high-temperature regions of the study area, which are mostly residential areas, are distributed in the southwest according to the temperature inversion results for the above five time points. The subhigh-temperature regions are mainly distributed in the plains and mountainous areas of the study area. The regions with the lowest temperatures are mostly located in water bodies and valleys. The main reason is that mountains receive more solar radiation than other regions, while valleys not only receive less solar radiation but also are affected by shadows. Therefore, the inversion temperature of mountains and plains are higher than those of valleys.

Comparing panels in Fig. 6(a)–(d) shows that the inversion results in Fig. 6(b) and (d) are generally higher than those in Fig. 6(a) and (c). The main reason is that the period of Fig. 6(b) and (d) is spring, but Fig. 6(a) and (c) represent late autumn and winter, which is in line with the local climate characteristics. Temperature anomaly regions in Fig. 6(a) and (e) show similar distributions, with the same characteristics as those

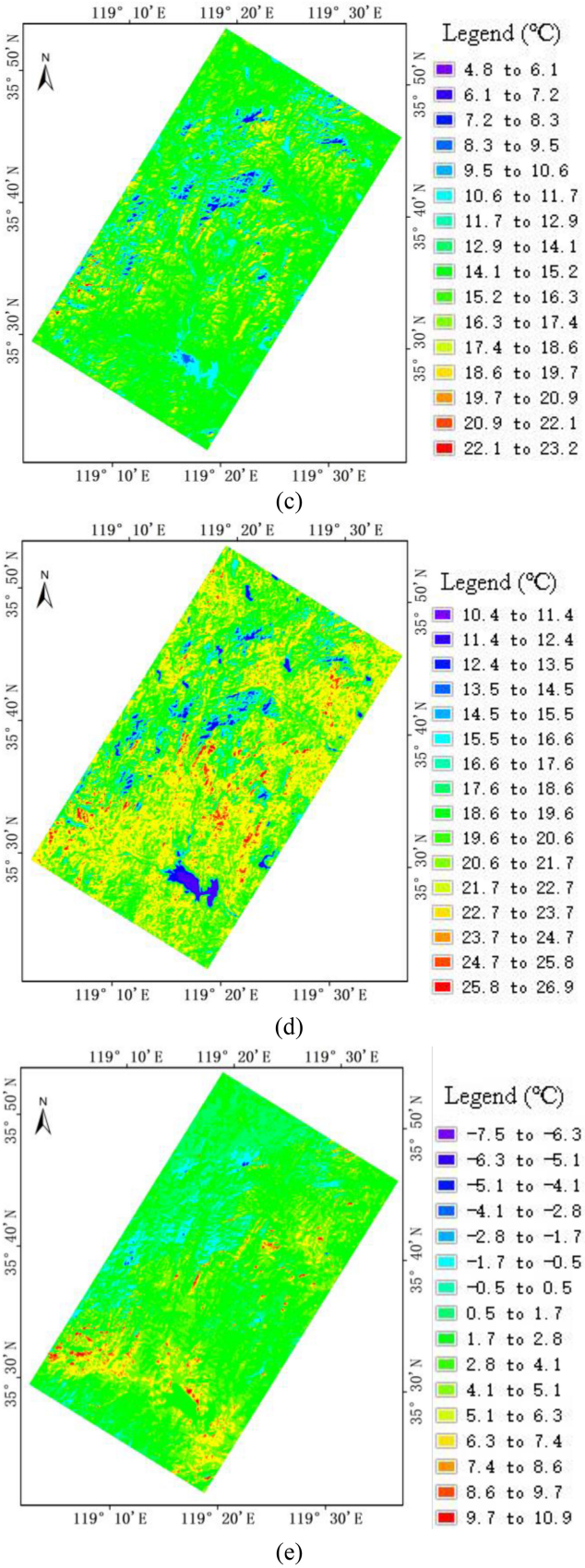

Fig. 6. (*Continued*) Temperature inversion results for each period. (c) Inversion results for November 8, 2014. (d) Inversion results for March 31, 2017. (e) Inversion results for February 1, 2019 (°C).

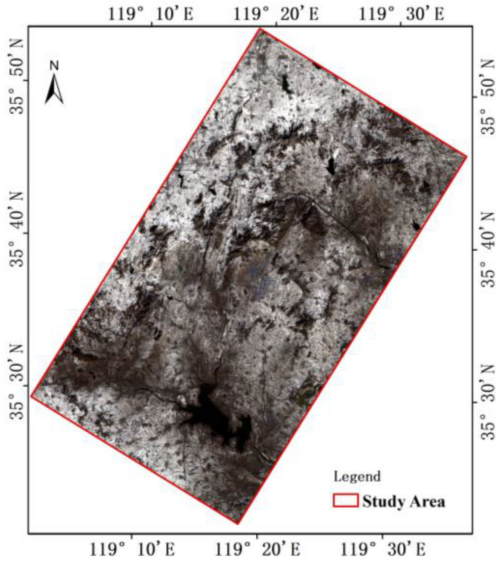

Fig. 7. True-color image of the study area on February 1, 2019.

in Fig. 6(b) and (d). The leading reason for this phenomenon is seasonal influence, which again demonstrates the flaw when using single-temporal data for geothermal exploration and the need for multitemporal TIR remote sensing data.

From Fig. 6(e), we can observe that the inversion results for temperature in this period are generally lower than those in other periods. Searching the local historical weather reveals that there was heavy snow in the study area in January 2019 and that snow remained in the study area until February 1, as shown in Fig. 7, thus leading to the inversion results shown in Fig. 6.

C. Classification in the Study Area

Considering the imaging quality of remote sensing images at different time points, this article uses remote sensing images from March 31, 2017, and divides the ground objects in the image into three categories according to the classification method mentioned above: bare ground, impervious surfaces, and water bodies. After the extraction of water bodies and impervious surfaces using the NDWI and NDBI, impervious surfaces are further eliminated by visual discrimination to reduce the influence of ground objects on the extraction of geothermal anomaly areas. The results are shown in Fig. 8(b). In Fig. 8, four typical small areas with impervious surfaces and water bodies are selected. Comparing the true-color image in Fig. 8(a) and the classification results in Fig. 8(b), the next step can be done under the condition that no obvious water bodies and impervious surfaces have missed detection.

D. Extraction of Abnormal Geothermal Areas Based on the Proposed Method

After completing the temperature inversion work and removing the influence of water bodies and impervious surfaces, the locations that have high temperatures at each time point are selected as the temperature anomaly points. In total, seven

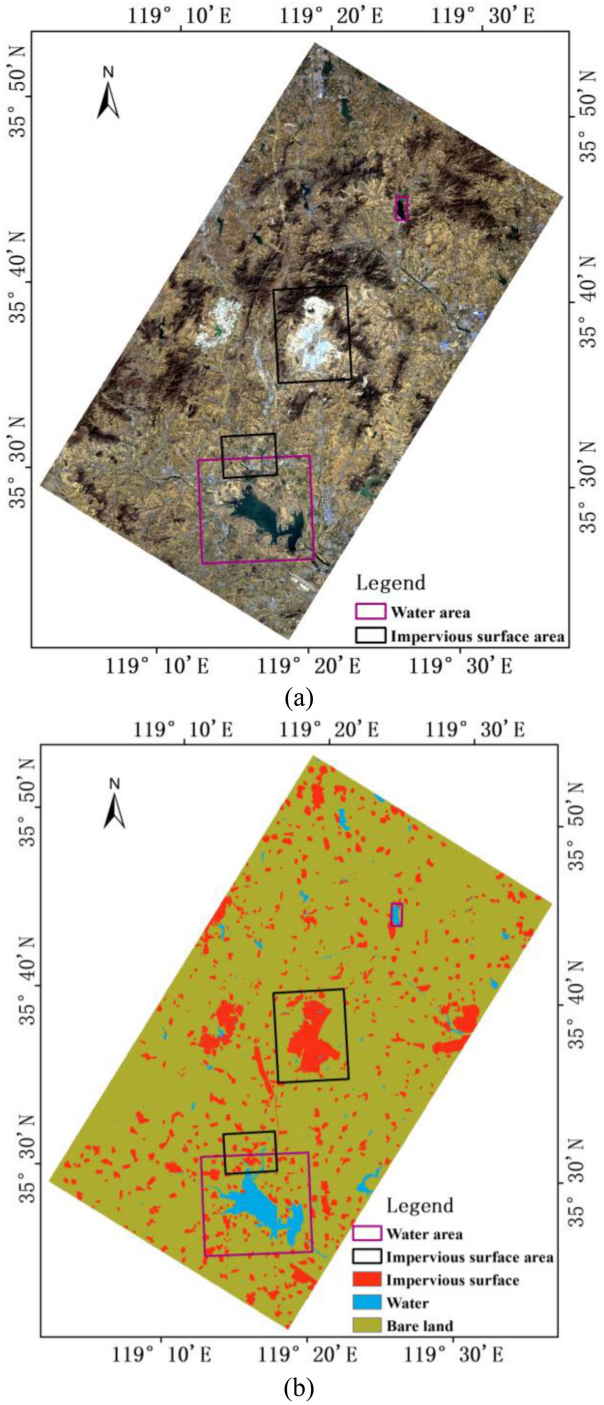

Fig. 8. Classification experiment. (a) True-color image of the study area on March 31, 2017. (b) Classification results of the study area.

temperature anomaly points are selected. The specific geographical distribution is shown in Fig. 9. The green dots are five geothermal anomalies selected based on 150 geothermal wells combined with the local geological structure, and the yellow dots are temperature anomaly points. Comparing the locations of temperature anomaly points with those of geothermal anomaly points reveals that the distributions between them are relatively close. Two areas are delineated in Fig. 9. In these two areas,

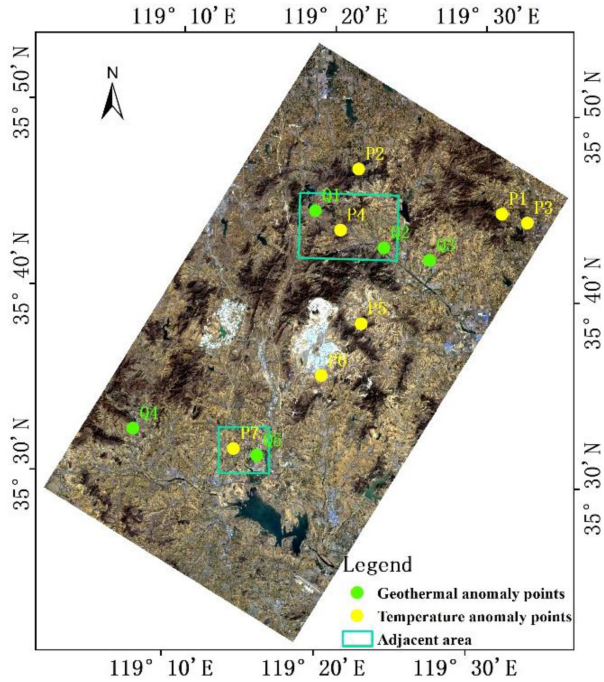

Fig. 9. Locations of the geothermal anomaly points and temperature anomaly points.

the temperature anomaly points and the geothermal anomaly points have the most similar distributions. The distance between temperature anomaly point P7 and geothermal anomaly point Q5 is less than 2.5 km, which is a very short distance considering the size of the study area and the geothermal characteristics.

Based on the proposed method, the Canny edge detector is used to extract the temperature anomaly areas in each period, and the areas are superimposed to obtain the geothermal anomaly areas based on the proposed method. The spatial locations of the thermal anomaly areas are shown in Fig. 10.

Fig. 10 shows that most of the temperature anomaly points and geothermal anomaly points are located inside or near the geothermal anomaly areas detected based on the proposed method, including temperature anomaly points P1, P3, P4, P5, and P6 and geothermal anomaly points Q1 and Q4.

V. Discussion

A. Geological Structural Analysis of the Study Area

Under the action of the north-northeast (NNE)-trending principal compressive stress in North China, the Yishu fault zone, and nearby fault zones are all NNE-trending faults. The faults in other directions are mostly secondary faults related to the activity of the Yishu fault zone, which is characterized by dextral strike-slip movement. Since the start of the Quaternary, the study area has entered a period of neotectonic activity, and several active faults have appeared. Fragmentation and fault gouge/active faults have developed on each of the main faults, although there are still partially inactive sections.

New and old strata and old structures can be cut by new structural faults because of the times of formation. New structures

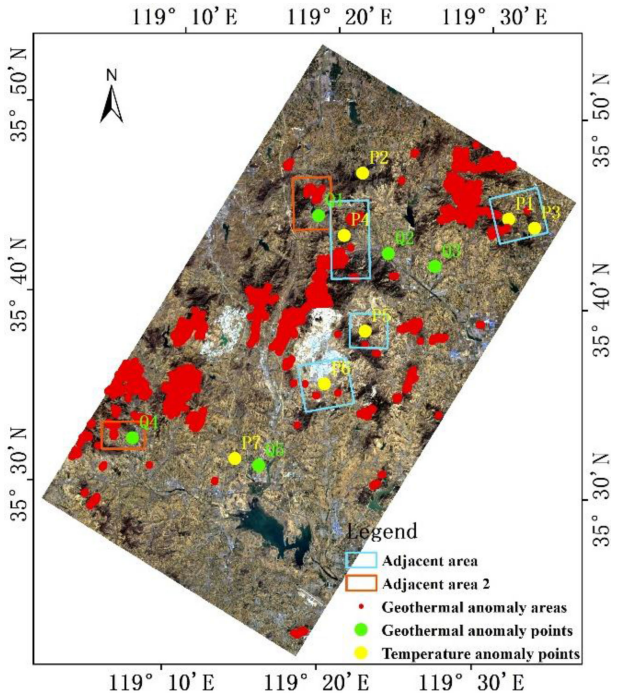

Fig. 10. Locations of the geothermal anomaly areas.

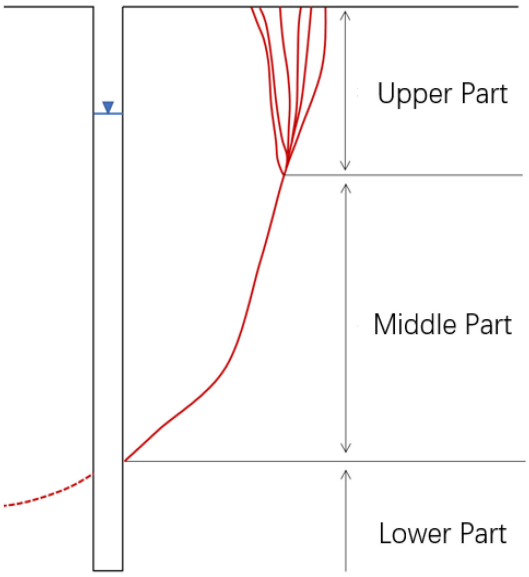

Fig. 11. Vertical distribution of new faults.

are generally unconsolidated and have good opening properties, which provide favourable conditions for surface water infiltration and replenishment. Fig. 11 shows the vertical zoning of the neotectonic fault zone. The upper part of the new fault is a densely structured joint zone or a weathered zone of joint fissures. The area is dense with joints and strong weathering. The groundwater is mainly characterized by vertical movement. The middle part is the main part, which is the main fault zone or cavity fissure zone. This zone is the most water-rich section of the fault zone; it has the most water and the best water quality.

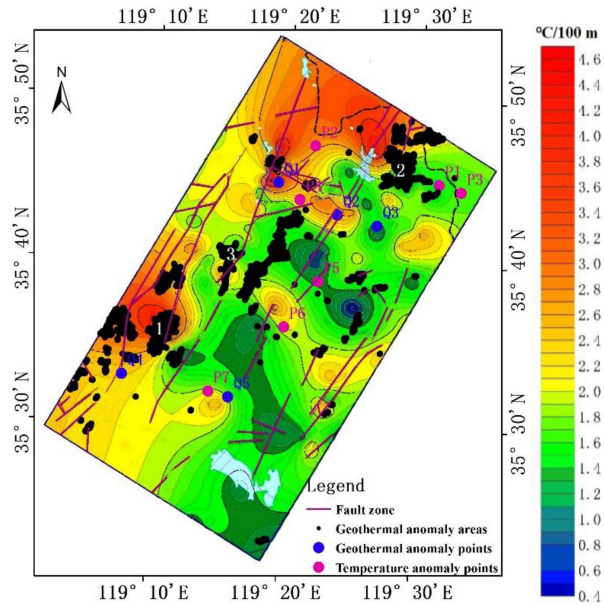

Fig. 12. Distribution of the major faults in the study area.

It is also the best spatial section for well drilling. The lower part is the closed fissure zone or fissure. In the lower part, the confining pressure in this area increases, the fissures are slowly closed, the groundwater flow rate is slow, the salinity is high, and the fissures are filled.

The NNE-trending faults in the study area are mainly compressional-torsional faults. There is thick fault mud in the middle of the section, which plays a role in blocking water. However, rock fragmentation zones are present on both sides of the section with gaps in the middle, and the water can move.

B. *Interpretation of Geothermal Anomaly Areas*

Synthesizing the geological structure in the study area leads to concluding that the main underground activity of groundwater in the study area is as follows. As the aboveground water moves down along the cracks of the new fault zone, the geothermal flow in the deep crust heats the water. As the gaps decrease, the flow direction of the water begins to change from vertical to horizontal. When water flows horizontally to the middle mud zone of the NNE-trending fault zone, the flow of water is blocked, and water can move only along the cracks beside the fault zone until it encounters a new vertical fault. The water then moves upwards with heat, so geothermal anomalies can be detected, forming a geothermal anomaly consistent with the trend of the fault zone. Therefore, the main NNE-trending fault in the study area plays a role in controlling heat. At the same time, most of the northwest-, northeast-, and nearly east-west-trending faults are tensile-torsional faults. The rocks in the belt are extensively broken, and structural breccias and structural lenses, which play a role in water conduction, have developed.

Comparing Figs. 10 with 12, we find that except for part of the geothermal anomaly areas along the fault zone, the rest of the geothermal anomaly areas are mainly distributed in various

mountainous areas, as most of the rocks on the mountains of the study area are volcanic rocks, while the main rock type on the plains is clastic sedimentary rock. As clastic rock is less dense than volcanic rock, there are many gaps filled with air. Moreover, the thermal conductivity of air is much lower than that of rock. Therefore, volcanic rock can conduct heat energy in the deep layers of the earth's crust better than clastic rock, and many geothermal anomalies are detected in mountainous areas.

In summary, three typical geothermal anomaly areas are selected as examples to analyze the geothermal anomaly areas in Fig. 12. Among these areas, there are many faults in area 1, and the geothermal trend along the main fault zone in this area is NNE. There are fewer faults in area 2 than in area 1, but the former is still interpreted as a geothermal anomaly area, mainly because there are more mountains in area 2. The thermal conductivity of the rocks in the mountains is higher than that of the rocks in the plains. Some detected geothermal anomaly areas need to be analysed in combination with these two situations. For example, in area 3, although the geothermal anomaly area is in the fault zone, its trend, which is mainly along the mountainous terrain, is not completely consistent with that of the fault zone. The geothermal anomaly area is dominated by the thermal conductivity of volcanic rocks.

Fig. 12 shows not only the spatial distribution of most of the geothermal anomaly areas in the study area along the local fault zones and mountains but also the distribution of the abnormal temperature points (P1, P5, P6, and P7) judged by visual interpretation, which also have the same geographic trend (NNE) as the local fault zone; thus, the geothermal anomaly area in the study area is affected by the trend of the main fault zone.

Fig. 12 shows that the high-value region in the northern region of the study area is not detected by the proposed method. Comparing Figs. 12 with 3, we find that there are few geothermal wells in the region. The main reason for this poor experimental result may be the inaccurate gradient caused by the shortage of inversion data in this region. Combining this information with the subsequent comparative experiments, we find that the results of the mean gradient method are similar to those of the proposed method.

C. Comparison With Other Methods

To demonstrate the reliability and superiority of the experimental results of the proposed method, a comparison is made with the mean grad method, which is a classic method used for studying surface TIR radiation. The method first calculates the mean values of all temperature inversion results and then determines the maximum absolute difference value between each point and adjacent pixels. To reduce the influence of impervious surfaces and water on geothermal detection based on the mean grad method, we remove impervious surfaces and water bodies in the result shown in Fig. 13(a). Based on the principle of the average gradient algorithm, the hotter the color is in the image, the more likely it is to be a geothermal anomaly. Fig. 13(a) shows that most geothermal anomaly points and temperature anomaly points are in the high-value area.

The comparison with the proposed method is shown in Fig. 13(b). We find that the geothermal anomaly area based on

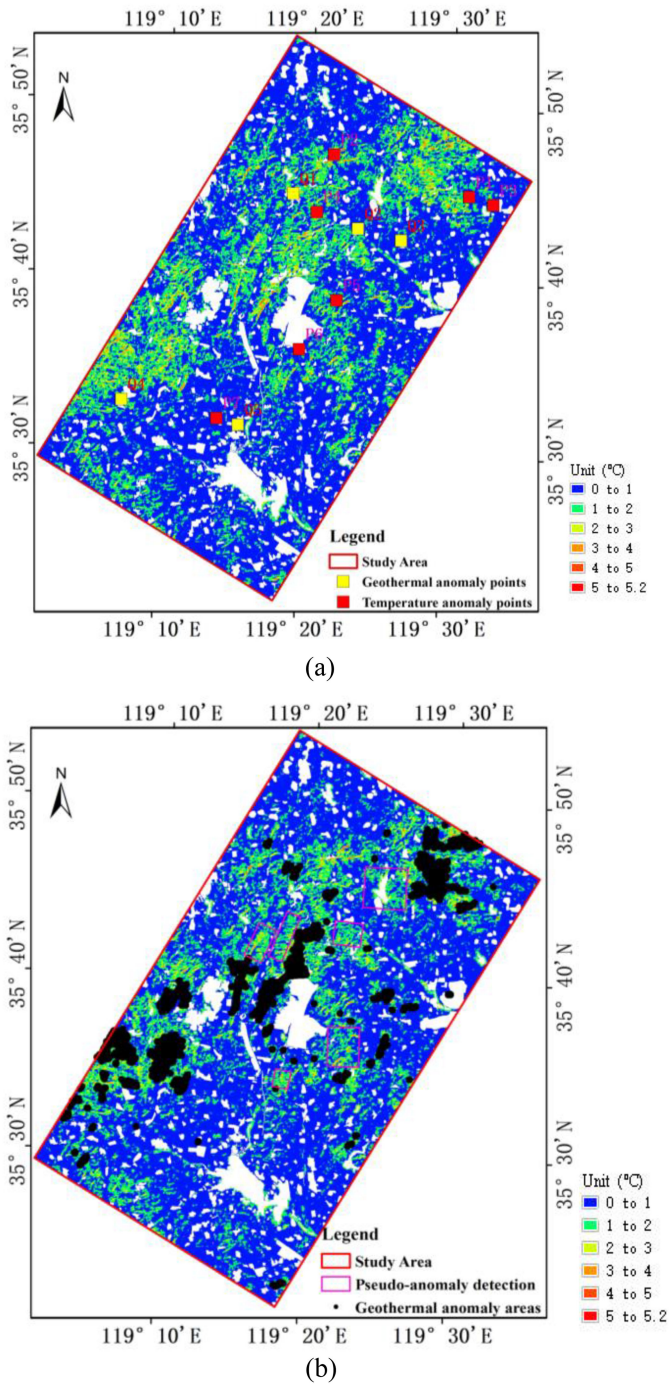

Fig. 13. Results of the comparative experiment. (a) Experimental results of the mean grad method. (b) Comparison with the proposed method.

the proposed method covers most of the anomaly areas extracted based on the mean grad method and is mainly distributed in high-value areas of the mean grad method, which again manifests the dependability of the proposed method. Comparing Figs. 13(b) and 12, we immediately observe that the geothermal anomaly areas extracted from the mean grad method are more extensive than those based on the proposed method. The main reason of this phenomenon is that the proposed method deletes some anomaly areas that are not stable at a particular time. The proposed method can not only delete some unstable geothermal

anomaly areas but also eliminate some pseudo-anomaly areas, which is shown in Fig. 13(b). Therefore, we conclude that the proposed method can effectively delete some pseudo-anomaly areas under the premise of ensuring the extraction accuracy of geothermal anomaly areas.

It can also be seen that the distribution of high-temperature anomaly areas from the temperature inversion experiment for individual time points is different from that obtained by analysing the temperature inversion diagrams of each period in Fig. 6. Thus, there is a certain contingency to detecting geothermal anomalies using TIR remote sensing images for individual time points, and the geothermal anomaly areas extracted based on the spatio-temporal analysis method are more convincing.

D. Challenges of the Proposed Method

Extracting geothermal anomaly areas using TIR remote sensing data is not easy because there are many external interference factors in the extraction process. In this article, we mainly consider the influence of the distribution of features. In addition to the impact of features, many other factors influence the results. For example, solar radiation heats the ground. Therefore, the result of temperature inversion based on daytime data cannot show the geothermal distribution. This is why previous researchers used night-time data. From this article, we can also find that the terrain plays a negative role in the results. In the next study, we will attempt to use night-time TIR remote sensing data to extract geothermal anomaly areas while eliminating the influence of terrain.

VI. Conclusion

In this study, multitemporal Landsat 8 remote sensing images are used to detect geothermal anomaly areas in the Jiaonan uplift in the Yishu fault zone. This article uses multitemporal TIR remote sensing images to carry out LST inversion experiments in the study area. After excluding the impact of impervious surfaces, water, and vegetation on the detection of geothermal anomaly areas, the locations of temperature anomaly points and geothermal anomaly points are similar.

Based on the analysis of the geothermal anomaly areas obtained by the method proposed in this study, the main reason behind this similarity is that the NNE-trending faults in the study area have heat control properties. Therefore, in subsequent geothermal exploration work, the main exploration area can be located near the NNE-trending fault zone within the region, providing a direction for future geothermal research in the region.

Compared with other methods, the remote sensing detection method combined with temporal and spatial analysis not only can rapidly achieve geothermal detection over a wide range but also yields more reliable experimental results than geothermal anomaly detection methods using individual time points. In addition, the proposed method can delete some unstable geothermal anomaly areas and pseudo-anomaly areas without reducing the accuracy of extracting geothermal anomaly areas. In summary, the spatio-temporal analysis method is more effective and faster than traditional geological methods for geothermal anomaly detection and saves considerable time and labour costs.

Acknowledgment

The authors would like to thank the editors and the National Aeronautics and Space Administration (NASA) for providing the satellite data.

References

[1] E. Barbier, "Geothermal energy technology and current status: An overview," *Renew. Sust. Energ. Rev.*, vol. 6, pp. 3–65, Jan. 2002.

[2] I. M. Nieto, D. Borge-Diez, C. Sáez Blázquez, A. F. Martín, and D. González-Aguilera, "Study on geospatial distribution of the efficiency and sustainability of different energy-driven heat pumps included in low enthalpy geothermal systems in Europe," *Remote Sens.,* vol. 12, pp. 1093–1109, Mar. 2020.

[3] C. Sáez Blázquez, P. Carrasco García, I. M. Nieto, M. Á. Maté-González, A. F. Martín, and D. González-Aguilera, "Characterizing geological heterogeneities for geothermal purposes through combined geophysical prospecting methods," *Remote Sens.,* vol. 12, pp. 1948–1965, Jun. 2020.

[4] M. P. Hochstein and S. Sudarman, "History of geothermal exploration in Indonesia from 1970 to 2000," *Geothermics,* vol. 37, pp. 220–266, 2008.

[5] D. T. Hodder, "Application of remote sensing to geothermal prospecting," *Geothermics,* vol. 2, pp. 368–380, Jan. 1970.

[6] M. F. Coolbaugh, C. Kratt, A. Fallacaro, W. M. Calvin, and J. V. Taranik, "Detection of geothermal anomalies using advanced spaceborne thermal emission and reflection radiometer (ASTER) thermal infrared images at Bradys Hot Springs, Nevada, USA," *Remote Sens. Environ.,* vol. 106, pp. 350–359, 2007.

[7] C. Haselwimmer and A. Prakash, *Thermal Infrared Remote Sensing of Geothermal Systems*, Dordrecht, Netherlands: Springer, 2013, pp. 453–473.

[8] F. van der Meer, C. Hecker, F. van Ruitenbeek, H. van der Werff, C. de Wijkerslooth, and C. Wechsler, "Geologic remote sensing for geothermal exploration: A review," *Int. J. Appl. Earth Obs.,* vol. 33, pp. 255–269, 2014.

[9] Y. M. Darge, B. T. Hailu, A. A. Muluneh, and T. Kidane, "Detection of geothermal anomalies using Landsat 8 TIRS data in Tulu Moye geothermal prospect, main Ethiopian rift," *Int. J. Appl. Earth Obs.,* vol. 74, pp. 16–26, 2019.

[10] M. Silvestri *et al.*, "Monitoring of surface temperature on Parco Delle Biancane (Italian geothermal area) using optical satellite data, UAV and field campaigns," *Remote Sens.,* vol. 12, pp. 2018–2033, Jun. 2020.

[11] M. Silvestri, V. Romaniello, S. Hook, M. Musacchio, S. Teggi, and M. F. Buongiorno, "First comparisons of surface temperature estimations between ECOSTRESS, ASTER and Landsat 8 over Italian volcanic and geothermal areas," *Remote Sens.,* vol. 12, pp. 184–194, Jan. 2020.

[12] R. G. Vaughan, L. P. Keszthelyi, A. G. Davies, D. J. Schneider, C. Jaworowski, and H. Heasler, "Exploring the limits of identifying subpixel thermal features using ASTER TIR data," *J. Volcanol. Geoth. Res.*, vol. 189, pp. 225–237, 2010.

[13] H. Heasler and C. Jaworowski, "Hydrothermal monitoring of Norris Geyser Basin, Yellowstone National Park, USA, using airborne thermal infrared imagery," *Geothermics*, vol. 72, pp. 24–46, 2018.

[14] E. Lagios, S. Vassilopoulou, V. Sakkas, V. Dietrich, B. N. Damiata, and A. Ganas, "Testing satellite and ground thermal imaging of low-temperature fumarolic fields: The dormant Nisyros volcano (Greece)," *ISPRS J. Photogramm.,* vol. 62, pp. 447–460, 2007.

[15] Y. Zhou, "The application of thermal infrared remote sensing techniques in geothermal surveying," *Remote Sens. Land Resour.*, vol. 10, no. 4, pp. 24–28, 1998.

[16] L. González and P. Rodríguez-Gonzálvez, "Detection of geothermal potential zones using remote sensing techniques," *Remote Sens. (Basel, Switzerland),* vol. 11, no. 20, pp. 2403–2422, Jan. 2019.

[17] M. J. Hellman and M. S. Ramsey, "Analysis of hot springs and associated deposits in Yellowstone National Park using ASTER and AVIRIS remote sensing," *J. Volcanol. Geoth. Res.,* vol. 135, pp. 195–219, 2004.

[18] B. Tian, L. Wang, K. Kashiwaya, and K. Koike, "Combination of well-logging temperature and thermal remote sensing for characterization of geothermal resources in Hokkaido, Northern Japan," *Remote Sens.,* vol. 7, pp. 2647–2667, Mar. 2015.

[19] Q. Qin, N. Zhang, P. Nan, and L. Chai, "Geothermal area detection using landsat ETM+ thermal infrared data and its mechanistic analysis—A case study in Tengchong, China," *Int. J. Appl. Earth Obs.*, vol. 13, pp. 552–559, 2011.
[20] B. Yang, D. Wu, J. Lai, and P. Tang, "The application of remote sensing technology to the study and forecast of terrestrial heat resources in Southwestern Tengchong Yunnan Province," *Remote Sens. Land Resour.*, vol. 15, pp. 23–26, 2003.
[21] T. R. Walter, A. Belousov, M. Belousova, T. Kotenko, and A. Auer, "The 2019 eruption dynamics and morphology at Ebeko volcano monitored by unoccupied aircraft systems (UAS) and field stations," *Remote Sens.,* vol. 12, pp. 1961–1980, Jun. 2020.
[22] S. V. Cherkasov, A. M. Farkhutdinov, D. P. Rykovanov, and A. A. Shaipov, "The use of unmanned aerial vehicle for geothermal exploitation monitoring: Khankala field example," *J. Sustain. Develop. Energy, Water Environ. Syst.,* vol. 6, no. 2, pp. 351–362, 2018.
[23] A. Nishar, S. Richards, D. Breen, J. Robertson, and B. Breen, "Thermal infrared imaging of geothermal environments and by an unmanned aerial vehicle (UAV): A case study of the Wairakei–Tauhara geothermal field, Taupo, New Zealand," *Renew. Energ.*, vol. 86, pp. 1256–1264, 2016.
[24] G. Norini *et al.*, "Structural analysis and thermal remote sensing of the Los Humeros volcanic complex: Implications for volcano structure and geothermal exploration," *J. Volcanol. Geoth. Res.,* vol. 301, pp. 221–237, 2015.
[25] H. Chan, C. Chang, and P. D. Dao, "Geothermal anomaly mapping using landsat ETM+ data in Ilan plain, Northeastern Taiwan," *Pure Appl. Geophys.,* vol. 175, pp. 303–323, 2018.
[26] W. Wu, L. Zou, X. Shen, S. Lu, N. Su, and F. Kong, "Thermal anomalies associated with faults: A case study of the Jinhua-Quzhou basin of Zhejiang Province, China," *Int. J. Remote Sens.*, vol. 33, no. 6, pp. 1850–1867, 2012.
[27] G. C. Miliaresis, "Regional thermal and terrain modelling of the afar depression from MODIS multi-temporal monthly night LST data," *Int. J. Remote Sens.*, vol. 30, no. 9, pp. 2429–2436, 2009.
[28] D. Zouzias, G. C. Miliaresis, and K. St. Seymour, "Probable regional geothermal field reconnaissance in the Aegean region from modern multi-temporal night LST imagery," *Environ. Earth Sci,* vol. 62, pp. 717–723, 2011.
[29] S. Piscitelli, N. Pergola, G. D. Bello, and V. Tramutoli, "Robust satellite techniques for remote sensing of seismically active areas," *Ann. Geophys.-Italy.,* vol. 44, pp. 295–312, 2001.
[30] S. Chen, J. Ma, P. Liu, L. Liu, and G. Chen, "Mean grad method (MGM) for distinguishing information of current tectonic activity from thermal radiation field of land surface," *Seismol. Geol.,* vol. 27, pp. 661–668, 2005.
[31] L. Song *et al.*, "Provenance of cretaceous Dasheng group Malanggou formation in the mid-part of the Yishu fault zone, Shandong Province, China," *Arab. J. Geosci.,* vol. 12, no. 771, 2019.
[32] Q. Deng *et al.*, "Evaluation of favourable hot dry rock areas in the east of the Yishu fault zone in China," *Aust. J. Earth Sci.,* vol. 68, no. 2, pp. 1–17, Jan. 2020.
[33] W. Schroeder, P. Oliva, L. Giglio, B. Quayle, E. Lorenz, and F. Morelli, "Active fire detection using Landsat-8/OLI data," *Remote Sens. Environ.,* vol. 185, pp. 210–220, 2016.
[34] D. P. Roy *et al.*, "Landsat-8: Science and product vision for terrestrial global change research," *Remote Sens. Environ.,* vol. 145, pp. 154–172, 2014.
[35] A. Bendib, H. Dridi, and M. I. Kalla, "Contribution of Landsat 8 data for the estimation of land surface temperature in Batna city, Eastern Algeria," *Geocarto Int.,* vol. 32, pp. 503–513, 2016.
[36] G. Rongali, A. K. Keshari, A. K. Gosain, and R. Khosa, "Split-Window algorithm for retrieval of land surface temperature using Landsat 8 thermal infrared data," *J. Geovisualization Spatial Anal.,* vol. 2, no. 14, 2018.
[37] V. García-Santos, J. Cuxart, D. Martínez-Villagrasa, M. Jiménez, and G. Simó, "Comparison of three methods for estimating land surface temperature from Landsat 8-TIRS sensor data," *Remote Sens.,* vol. 10, pp. 1450, Sep. 2018.
[38] X. Yu, X. Guo, and Z. Wu, "Land surface temperature retrieval from Landsat 8 TIRS—Comparison between radiative transfer equation-based method, split window algorithm and single channel method," *Remote Sens.,* vol. 6, pp. 9829–9852, Oct. 2014.
[39] Y. Wang, J. Zhou, M. Li, and X. Zhang, "Validation of Landsat-8 TIRS LAND surface temperature retrieved from multiple algorithms in an extremely arid region," in *Proc. IEEE Int. Geosci. Remote Sens. Symp. (IGARSS)*, 2016, pp. 6934–6937.
[40] J. A. Sobrino *et al.*, "Land surface emissivity retrieval from different VNIR and TIR sensors," *IEEE T. Geosci. Remote.,* vol. 46, no. 2, pp. 316–327, Feb. 2008.
[41] J. C. Jimenez-Munoz, J. Cristobal, J. A. Sobrino, G. Soria, M. Ninyerola, and X. Pons, "Revision of the single-channel algorithm for land surface temperature retrieval from Landsat thermal-infrared data," *IEEE T. Geosci. Remote.,* vol. 47, no. 1, pp. 339–349, Jan. 2009.
[42] Y. Zhang, I. O. A. Odeh, and C. Han, "Bi-temporal characterization of land surface temperature in relation to impervious surface area, NDVI and NDBI, using a sub-pixel image analysis," *Int. J. Appl. Earth Obs.,* vol. 11, pp. 256–264, 2009.
[43] C. Haselwimmer, A. Prakash, and G. Holdmann, "Geothermal exploration at pilgrim hot springs, Alaska using airborne thermal infrared remote sensing," in *Proc. Geothermal Resource Council Annu. Meeting,* San Diego, CA, USA, pp. 805–810, 2011.

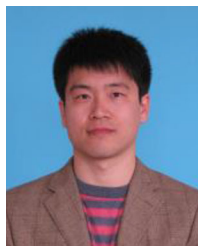

Shanwei Liu received the Ph.D. degree in Environmental Science from Yantai Institute of Coastal Zone Research, Chinese Academy of Sciences, Beijing, China, in 2011.

He is currently an Assistant Professor with the College of Oceanography and Space Informatics, China University of Petroleum (East China), Qingdao, China. He has authored or coauthored more than ten high-level papers, and is the inventor or coinventor of five patents. His research interests include satellite altimetry, ocean remote sensing, and GIS application.

Chuanlong Ye received the bachelor's degree in Surveying and Mapping from the School of Geosciences, China University of Petroleum (East China), Qingdao, China, in 2019. He is currently working toward the graduate degree in Surveying and Mapping at the College of Oceanography and Space Informatics, China University of Petroleum (East China), Qingdao, China.

His research interests include hyperspectral image processing and sparse unmixing

Qinting Sun received the bachelor's degree in Surveying and Mapping from the College of Information Science and Engineering, Shandong Agricultural University, Tai'an, China, in 2016. She is currently working toward the graduate degree in Computer Technology Resources Information Engineering at the School of Geosciences, China University of Petroleum (East China), Qingdao, China.

Her research interests include satellite altimetry, deep learning, and sea level change.

Mingming Xu (Member, IEEE) received the B.S. degree in surveying and mapping engineering from the China University of Petroleum, Qingdao, China, in 2011, and the Ph.D. degree in photogrammetry and remote sensing from the State Key Lab of Information Engineering in Surveying, Mapping and Remote Sensing, Wuhan University, Wuhan, China, in 2016.

She is currently a Lecturer with the College of Oceanography and Space Informatics, China University of Petroleum. Her research interests include hyperspectral image processing and intelligent computation.

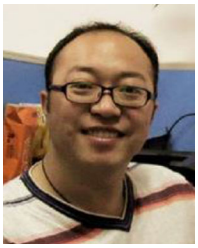

Zhongfeng Duan received the Ph.D. degree in Geology from the Institute of Geology and Geophysics, Chinese Academy of Sciences, Beijing, China, in 2011.

He is currently a Lecturer with the School of Geosciences, China University of Petroleum, Qingdao, China. He has authored or coauthored more than ten high-level papers, and he is the inventor or coinventor of five patents. His research interests include hydrogeology and geothermics.

Hui Sheng received the Ph.D. degree in Geological Resources and Geological Engineering from the China University of Petroleum, Qingdao, China, in 2010.

He is currently an Assistant Professor with the College of Oceanography and Space Informatics, China University of Petroleum (East China), Qingdao, China. He has authored or coauthored seven high-level papers, and has undertaken a number of scientific research projects. His research interests include ocean remote sensing and photogrammetry.

Jianhua Wan received the Ph.D. degree in Surveying and Mapping from Wuhan University, Wuhan, China, in 2001.

He is currently a Professor with the College of Oceanography and Space Informatics, China University of Petroleum (East China), Qingdao, China. He has authored or coauthored more than 30 high-level papers, and is the inventor or coinventor of five patents. His research interests include geographic information, ocean remote sensing, and smart city.

Dr. Wan is the Director of the Chinese Society for Geodesy, Photogrammetry, and Cartography (CSGPC), a member of the Theory and Method Working Committee of China Association for Geographic Information System Society, a member of the Engineering Survey Special Committee of the Engineering Surveying Special Committee of CSGPC, a member of the Oceanology and Limnology Information Technology Special Committee of Chinese Society for Oceanology and Limnology, and the Vice Chairman of the Smart City Working Committee of CSGPC. He was also the Editorial Board Member of the GeomaticsWorld and the Instructor of Huitiandi, a well-known WeChat platform in the field of surveying and mapping geographic information. He was also the Evaluation Expert of National Science and Technology and the recipient of the National Science and Technology Award, Provincial Science and Technology Award, and National Natural Science Foundation.